Design and fabrication of 3D-printed patient-specific soft tissue and bone phantoms for CT imaging

Kai Mei[1*], Pouyan Pasyar[1], Michael Geagan[1], Leening P. Liu[1,2], Nadav Shapira[1], Grace J. Gang[1,3], J. Webster Stayman[3], and Peter B. Noël[1,4]

[1]Department of Radiology, Perelman School of Medicine, University of Pennsylvania, Philadelphia, PA, USA.

[2]Department of Bioengineering, University of Pennsylvania, Philadelphia, PA, USA.

[3]Department of Biomedical Engineering, Johns Hopkins University, Baltimore, MD, USA.

[4]Department of Diagnostic and Interventional Radiology, School of Medicine & Klinikum rechts der Isar, Technical University of Munich, 81675 München, Germany.

Corresponding Authors: Kai Mei *, Email: kai.mei@pennmedicine.upenn.edu

Peter B. Noël, Email: pbnoel@upenn.edu

Abstract

The objective of this study is to create patient-specific phantoms for computed tomography (CT) that have realistic image texture and densities, which are critical in evaluating CT performance in clinical settings. The study builds upon a previously presented 3D printing method (PixelPrint) by incorporating soft tissue and bone structures. We converted patient DICOM images directly into 3D printer instructions using PixelPrint and utilized stone-based filament to increase Hounsfield unit (HU) range. Density was modeled by controlling printing speed according to volumetric filament ratio to emulate attenuation profiles. We designed micro-CT phantoms to demonstrate the reproducibility and to determine mapping between filament ratios and HU values on clinical CT systems. Patient phantoms based on clinical cervical spine and knee examinations were manufactured and scanned with a clinical spectral CT scanner. The CT images of the patient-based phantom closely resembled original CT images in texture and contrast. Measured differences between patient and phantom were less than 15 HU for soft tissue and bone marrow. The stone-based filament accurately represented bony tissue structures across different X-ray energies, as measured by spectral CT. In conclusion, this study demonstrated the possibility of extending 3D-printed patient-based phantoms to soft tissue and bone structures while maintaining accurate organ geometry, image texture, and attenuation profiles.

Keywords: 3D printing, computed tomography, phantoms, bone imaging, quality assurance.

Introduction

In computed tomography (CT) research and clinical practice, anthropomorphic and geometric phantoms play a crucial role. Highly accurate, customizable, and realistic phantoms are particularly valuable for a variety of purposes, including maintenance, optimization, and development of software and hardware components of scanners. In recent years, there have been significant advancements in three-dimensional (3D) printing technology, resulting in numerous studies on 3D-printed patient-based phantoms for medical imaging [1]–[5]. Compared to conventional phantoms, 3D-printed phantoms are highly accessible, customizable, and cost-effective. For example, inexpensive and widely available fused deposition modeling (FDM) printers can create high-quality anthropomorphic phantoms that accurately depict human anatomy at reasonable costs.

Conventional 3D printing techniques prioritize the replication of object and organ shapes. Typically, these approaches include segmenting organs of interest from CT scans according to their specific densities (HU), converting the results into surface meshes (STL files), 3D-printing each object separately, and then assembling them into a complete phantom [3], [4], [6], [7]. However, each 3D-printed component has a uniform Hounsfield unit (HU), resulting in phantoms with lacking realistic image textures because their HUs cannot be modulated pixel-by-pixel [8]–[11]. Furthermore, the lack of natural transitions between different regions, e.g., organs, leads to loss of detail. A promising alternative is to directly translate digital imaging and communications in medicine (DICOM) image data into G-code. G-code is a Computer Numerical Control (CNC) programming language. G-code instructions tell the printer to move in specific directions and at specific speeds to produce a specific shape or object. One means of controlling the density (as required for CT phantoms) is to vary the filament extrusion rate (per unit time) on a pixel-by-pixel basis while maintaining a constant printing speed. A similar approach was used by Okkalidis et al. [12]–[17]. in conjunction with edge detection and morphological operations to enhance and

separate organs. Such processes still yield segmentation errors and loss of small features. Altering the line width by varying the extrusion rate alone does not provide sufficient spatial resolution due to the inherently slow response time of the extrusion process. Our group recently developed PixelPrint [18], a methodology that combines a software tool as well as a standard FDM printer to create phantoms [19]–[23]. In PixelPrint, DICOM images of the original patient are directly converted into G-code on a pixel-by-pixel basis. In order to emulate attenuation at each voxel, density is modeled as a ratio of filament to voxel volume, generating partial volume effects. The filament ratio is continuously modified by varying the printing speed. Polylactic acid (PLA), a common printing filament, allows a print range approximately from -850 to 200 HU at different filament ratios, and has been used to print various patient-based lung phantoms [19].

In parallel, significant progress has been made in developing filament materials suitable for FDM printing in medical applications. Several studies have explored and compared different types of filament materials for printing human soft tissue and bones [24]–[27]. Conventional materials, such as PLA and acrylonitrile butadiene styrene (ABS), are widely available and easy to print with. They have densities ranging from 0.8 to 1.2 g/ml and can represent various human soft tissues for CT or X-ray examinations. Special materials, such as thermoplastic polyurethanes (TPU), can provide distinct physical properties to the print, i.e. durability, strength, and elasticity. Specifically for bone, materials tailored for clinical applications have been introduced for 3D-printed implants. They are biodegradable by the patient's osteoclasts. As a result, printed objects with such materials can be fused with the patient's bone, through remodeling during the osteo-cycle [28]–[30]. Additionally, denser PLA filament mixed with gravimetric powdered stone (PLA/Stone) has become commercially available. In previous studies, this type of filament has been utilized for printing phantoms for both diagnostic imaging and radiation therapy [8], [14], [31]–[35]. For printing even higher density objects, commercially available filament materials mixed with micro metal powders, i.e. iron or copper, have also been utilized in phantom studies [6].

This study optimized several aspects of the previously published PixelPrint technique, including filament line spacing and print speed. Furthermore, StoneFil filament, a type of PLA/Stone filament, was utilized to expand the density range of our phantoms in order to print bony structures. Our results illustrate that the PixelPrint technique can create realistic phantoms of the human spine and knee joint with surrounding soft tissue. The resulting phantoms achieved accurate geometry, image texture, and attenuation. Moreover, the presented phantoms exhibited similar spectral attenuation profiles to that of bone structures, which enables their use in various spectral CT applications.

Materials and Methods

2.1 PixelPrint and 3D printing

The previously published PixelPrint algorithm was used to create G-code from CT image data to produce 3D-printed phantoms [18]. Briefly, density information was extracted from the clinical patient images to generate filament lines that varied in width according to the HU of individual pixels. These lines were uniformly spaced within each layer and perpendicular on adjacent layers. By adjusting the filament line widths pixel-by-pixel, volumetric filament per unit space, or infill ratio, was varied despite only using one type of filament. These different infill ratios then produced different attenuation in CT images due to the partial volume effect.

In this study, the filament lines were equally spaced at 0.5 mm. The width of the filament line changed at resolution of 0.167 mm. The minimum and maximum line widths were 0.2 and 0.5 mm, corresponding to the infill ratio ranging between 40% and 100%, respectively. Keeping a constant extrusion rate, the print head traveled at varying speeds based on the width of the extruded filament line. The slowest speed was 180 mm/min for the widest width of 0.5 mm, while the fastest was 450 mm/min for the smallest width of 0.2 mm. Each layer had a uniform height of 0.2 mm. The resulting volumetric rate of filament extrusion during the whole print remained

constant at 18 mm^3/min. To prevent overlapping of lines in consecutive layers with the same filament line direction, an offset of 0.167 mm (1/3 of the 0.5 mm line spacing) was introduced.

All phantoms were printed with Lulzbot TAZ 6 or Sidekick 747 (Fargo Additive Manufacturing Equipment 3D, LLC Fargo, ND, USA), paired with M175 v2 tool heads and 0.40 mm steel nozzles. StoneFil filament (FormFutura, AM Nijmegen, the Netherlands) with a diameter 1.75 mm was utilized. The temperature of the nozzle was set at 200 °C and the bed was warmed to 50 °C to enhance adherence. Acceleration of the print head was to 500 mm/s^2 and the threshold (jerk setting) was 8 mm/s.

2.2 Phantom design

Micro-CT phantom. Three cylindrical phantoms were designed and produced using PixelPrint filament lines to examine their stability and reproducibility. These filament lines constructed a matrix smaller than the typical resolution limit of clinical CT scanners. Three phantoms were printed with identical G-code instructions. These phantoms are 60 mm in length and 20 mm in diameter. Each of them consists of four sections with different but homogeneous infill ratios (100%, 70%, 50% and 30%). StoneFil filament lines were printed at a spacing of 1 mm in all four sections but with corresponding line widths of 1.0, 0.7, 0.5, and 0.3 mm, respectively. A thin outer layer was added to the phantom for support, particularly for low infill ratio sections.

Calibration phantom. To compute the conversion between StoneFil filament infill ratios and HUs, a calibration phantom was designed. The phantom is a cylinder with a diameter of 10 cm and height of 1 cm. It consists of seven equally divided pie slice-shaped sections. Each section was printed at a fixed line spacing of 0.5 mm but with different filament line widths (0.2 - 0.5 mm), corresponding to seven infill ratios (40 -100%, with 10% intervals).

Cervical vertebrae phantom. Institutional Review Board (IRB) approved this retrospective study. A cervical vertebrae phantom was created based on a patient image volume (10 x 10 x 10 cm^3) that was acquired on a clinical CT scanner (Siemens SOMATOM Definition Edge, Siemens Healthcare GmbH, Erlangen, Germany) at a tube voltage of 120 kVp with a standard diagnostic protocol. Table 1 lists detailed acquisition and reconstruction parameters for the patient scan. The patient data consist of four cervical vertebrae (C4 to C7), including the trachea and esophagus. A circular region of interest with a diameter of 10 cm was cropped in axial slices to form the phantom. HUs were converted to infill ratios based on the calibration phantom.

Knee phantom. A knee phantom was similarly generated using a patient scan on a clinical dual-layer CT scanner (IQon spectral CT, Philips Healthcare, the Netherlands) at a tube voltage of 120 kVp, as detailed in Table 1. A circular region of interest with a diameter of 10 cm was cropped from the axial slices of the patient's left knee. HUs were then converted to infill ratios.

Table 1. Acquisition parameters of CT image for phantom generation

	Cervical vertebrae	*Knee*
Scanner model	Siemens SOMATOM Definition Edge	Philips iQon Spectral CT
Tube voltage	120 kVp	120 kVp
Tube current	105 mA	196 mA
Rotation time	1000 ms	1026 ms
Spiral pitch factor	0.8	Axial
Exposure	131 mAs	201 mAs
$CTDI_{vol}$	8.85 mGy	17.1 mGy
Collimation width	0.6 / 38.4 mm	0.625 / 40.0 mm
Slice thickness	0.6 mm	0.67 mm
Reconstruction filter	I26s\3	B
Field of view	99.75 x 99.75 mm^2	304 x 304 mm^2
Matrix size	228 x 228 $pixel^2$	512 x 512 $pixel^2$
Pixel spacing	0.4375 mm	0.5938 mm

Collimation width values are noted as single / total collimation width.

2.3 Data acquisition

Three micro-CT phantoms were separately scanned on a commercial micro-CT (U-CT system, MILabs, CD Houten, the Netherlands) with a tube voltage of 50 kVp. In addition, these phantoms were also scanned on a clinical dual-layer CT system (IQon spectral CT, Philips Healthcare, the Netherlands) at a tube voltage of 120 kVp with a high-resolution protocol and a small field-of-view of 100 mm. Additional acquisition and reconstruction parameters of the two scans are listed in Table 2. Micro-CT images were exported from the scanner and reprocessed with a multi-planar reconstruction algorithm (MPR) in Horos (Horos Project, Annapolis, MD, USA) to ensure filament lines were parallel to the axial plane.

Table 2. Scan protocols for the micro-CT phantom

	Micro-CT	Clinical CT
Scanner model	MILabs U-CT	Philips IQon Spectral CT
Tube voltage	50 kVp	120 kVp
Tube current	0.21 mA	130 mA
Rotation time	54 s	1.923 s
Spiral pitch factor	Axial scan	0.39
Exposure	11.3 mAs	250 mAs
$CTDI_{vol}$	69 mGy	16.4 mGy
Collimation width	-	0.625 / 40.0 mm
Slice thickness	0.08 mm	0.67 mm
Reconstruction filter	-	YC
Field of view	22.16 x 22.16 mm^2	100 x 100 mm^2
Matrix size	277 x 277 $pixel^2$	512 x 512 $pixel^2$
Pixel spacing	0.080 mm	0.195 mm

Collimation width values are noted as single / total collimation width.

The calibration, cervical vertebrae, and the knee phantom were scanned inside the QRM chest phantom (Quality Assurance in Radiology and Medicine GmbH, Möhrendorf, Germany) with the clinical dual-layer CT system. Protocol parameters matched those of the original clinical examination of the patient, with the same pixel spacing and slice thickness in Table 1. For the

cervical phantom, a 400 mg/ml QRM hydroxyapatite (HA) insert was additionally scanned with the phantom as a reference for bone mineral density. For both patient-based phantoms, additional high dose scans were performed at 1000 mAs while keeping the other scanning parameters the same. This high exposure scan was included to reduce noise for image quality comparisons.

2.4 Calibration and data analysis

For computing the conversion between HUs and infill ratios, mean and standard deviation HU values of seven areas were measured in the calibration phantom. Square regions of interest (ROI) of 19 x 19 pixel^2 (13 x 13 mm^2) were manually placed in each of the seven density regions within 10-mm-thick center of the phantom. A linear regression was computed, and the resulting Pearson's correlation coefficient (r) was reported. All measurements were performed on a workstation with ImageJ (U. S. National Institutes of Health, https://imagej.nih.gov), and all analyses were computed with Python (Python Software Foundation, https://www.python.org/).

For the cervical vertebrae phantom and the knee phantom, CT images were exported from the scanner and registered to the original patient data (2D-wise) using the OpenCV Library (Open Source Computer Vision Library [36], https://opencv.org). Mean and standard deviation in regions of interest for different tissue types were measured. Line profiles of the phantom scan were also compared with the original patient scan. Additionally, virtual monoenergetic images from 40 to 200 keV were extracted to quantify the spectral response of the bone regions within the patient-based phantoms.

Results

The high reproducibility of PixelPrint was demonstrated by comparing three identically manufactured phantoms (Figure 1). In micro-CT scans of the phantoms, the grid-like structures generated by PixelPrint were clearly visible. Filament lines printed within each region had equal spacings of 1 mm and a constant width in all three phantoms in the micro-CT scans. The layered

structure with introduced offsets (1/3 of 1 mm line spacing) was distinctly visible in orthogonal views (Figure 1f, 1g, 1h). However, in clinical CT scans with high resolution protocols, these structures were imperceptible because their size was smaller than the detector resolution. Instead, they appeared as constant regions due to partial volume effect (Figure 1e). Furthermore, both the micro-CT and clinical CT scans showed a high linear relationship between infill ratios and mean HUs in four regions (Pearson's correlation coefficient r = 0.984 and 0.982, respectively).

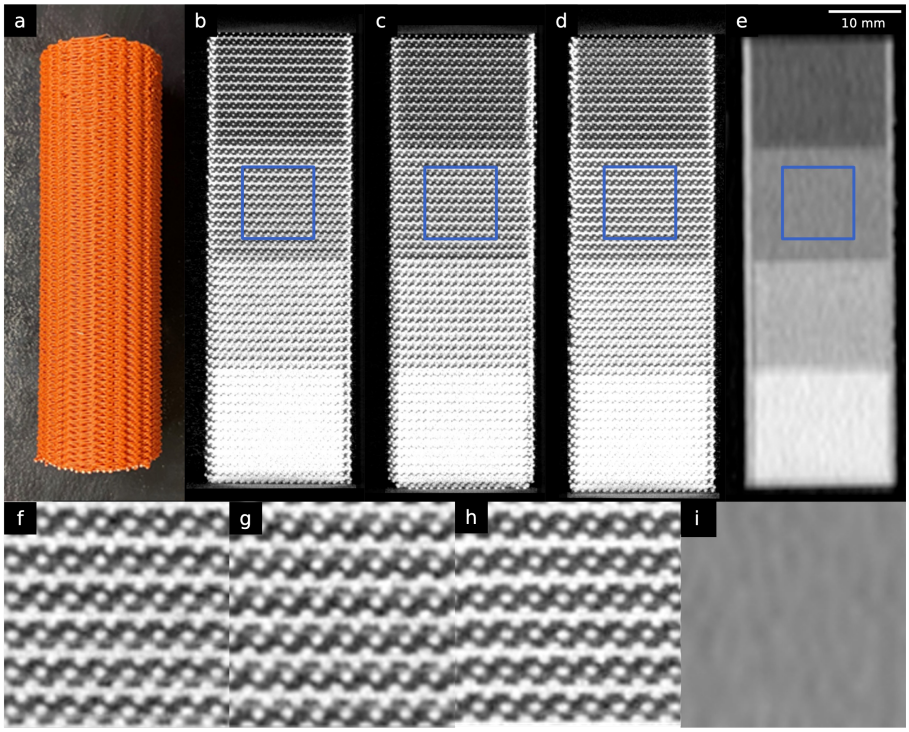

Figure 1. Micro-CT phantoms. (a) A photo of one of the three printed micro-CT phantoms. (b)-(d) Orthogonal views of the three different micro-CT phantoms scanned on a micro-CT. (e) Clinical CT image of one of the micro-CT phantoms. (f) – (i) Zoomed views of the regions enclosed by blue squares in (b) - (e). Window level/width are -750/3500 HU for micro-CT images and 0/2000 HU for clinical CT images.

In the calibration phantom, the infill ratio and HU also demonstrated excellent linearity across the seven regions (Figure 2). The highest infill ratio (100%) region measured 851 ± 24.7 HU, while the lowest infill ratio (40%) measured -227 ± 25.4 HU. Pearson's correlation coefficient of greater than 0.99 indicated a very high positive linear correlation between infill ratios and HUs. A conversion equation was computed for converting HU to infill ratio:

224 $$5.5258 \text{ x } 10^{-4} \times \text{ HU } + \text{ 0.52797 } = \text{ Infill Ratio (\%)}$$

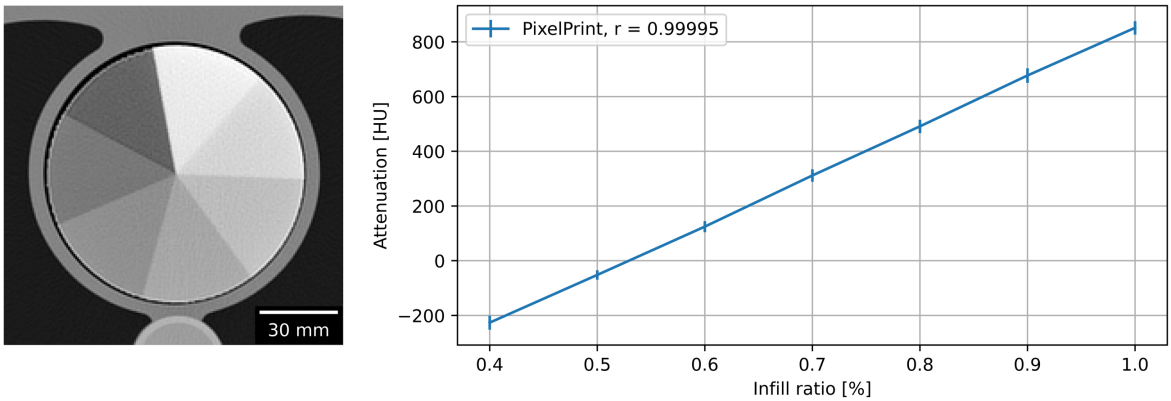

Figure 2. Linear correlation of filament infill ratio and HUs. (a) CT image of calibration phantom. Window level and width are 0 HU and 2000 HU. (b) Linear relationship between attenuation and infill ratio. Mean and standard deviation were measured in regions of interest in each area with a distinct infill ratio. Standard deviations are indicated with error bars.

225

226

227 Figure 3 shows the CT images of the cervical vertebrae phantom, while Figure 4 illustrates the
228 images of the knee phantom. The PixelPrint phantoms closely resembled the original CT images
229 in terms of contrast and features, with both the shape and the details inside the bones very well
230 reproduced. The image features in the high dose knee phantom scan appeared as sharp as the
231 original patient image.

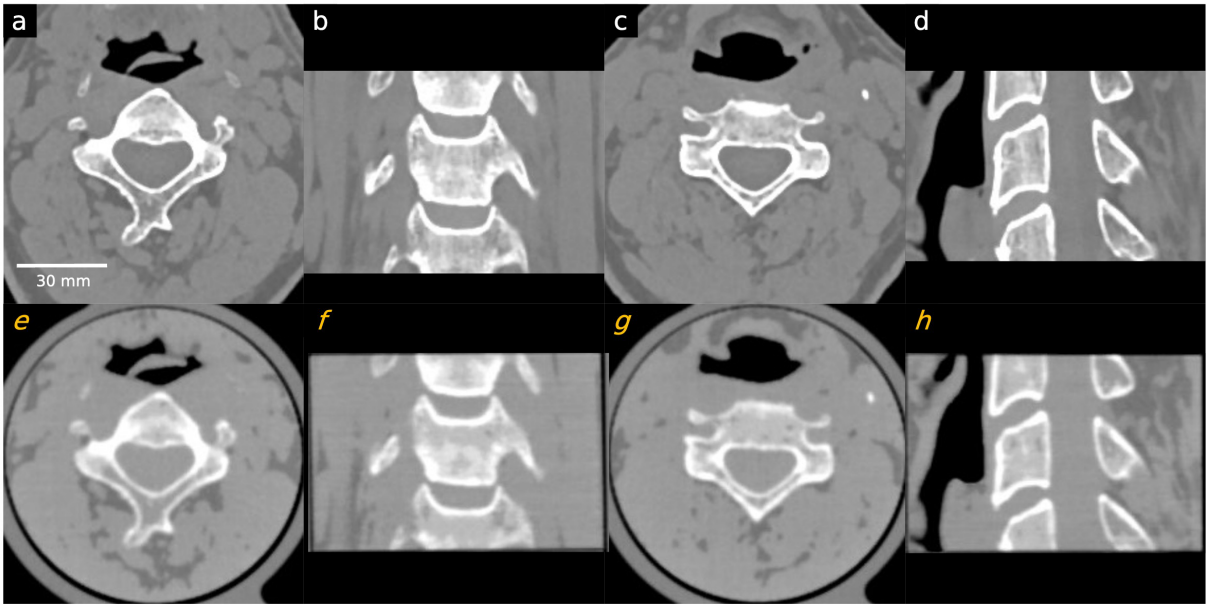

Figure 3. Comparison between patient CT images and the PixelPrint cervical phantom images. Images in the first row (a-d) are original DICOM images used to create the PixelPrint cervical phantom. Images on the second row (e-h) are the CT images of the phantom. All images have window level of 0 HU and width of 1200 HU. Sagittal and coronal images are not registered but are approximately at the same location.

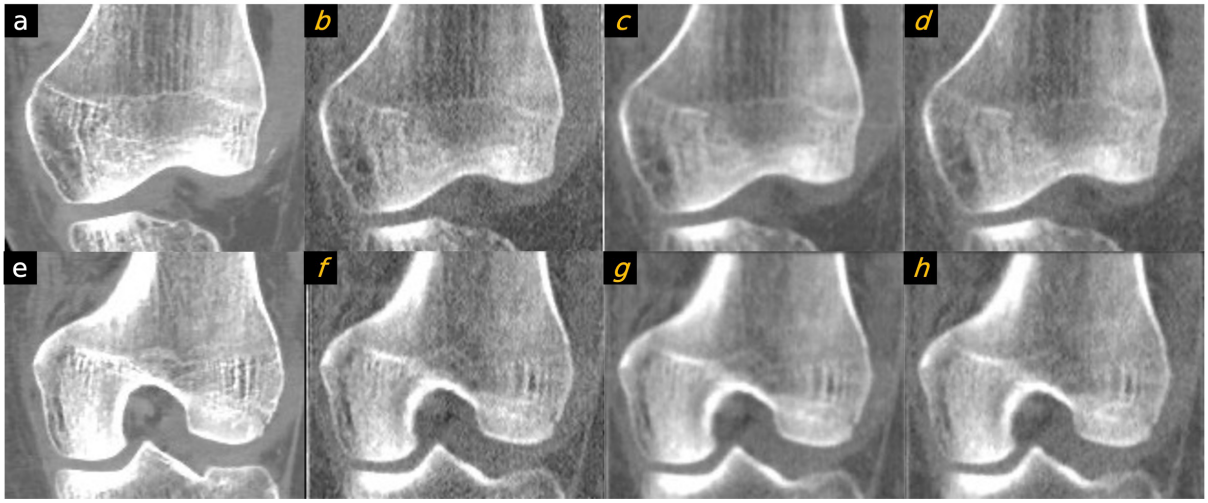

Figure 4. Comparison between patient image and the PixelPrint knee phantom. Images in the first column are original DICOM images used to create the PixelPrint knee phantom. Images on the second to fourth column are the CT images of the phantom: (b/f) high dose sharp kernel. (c/f) high dose standard kernel. (d/h) standard dose sharp kernel. All images have window level of 0 HU and width of 1200 HU. Images are not registered but are approximately at the same location.

Patient phantoms showed high accuracy. Line profiles indicated a match in HUs between the CT image of the cervical vertebrae phantom and the patient data (Figure 5). Quantitative

measurements in selected regions of trabecular and cortical bones, as well as adipose- and muscle-like soft tissues, are provided in Table 3. Measurements indicated that, except for the cortical bone, all other regions had differences of less than 15 HU compared to the patient image. Due to the density limitations of the utilized filament, HUs for the cortical bone (region 3 in Figure 6) were lower than expected.

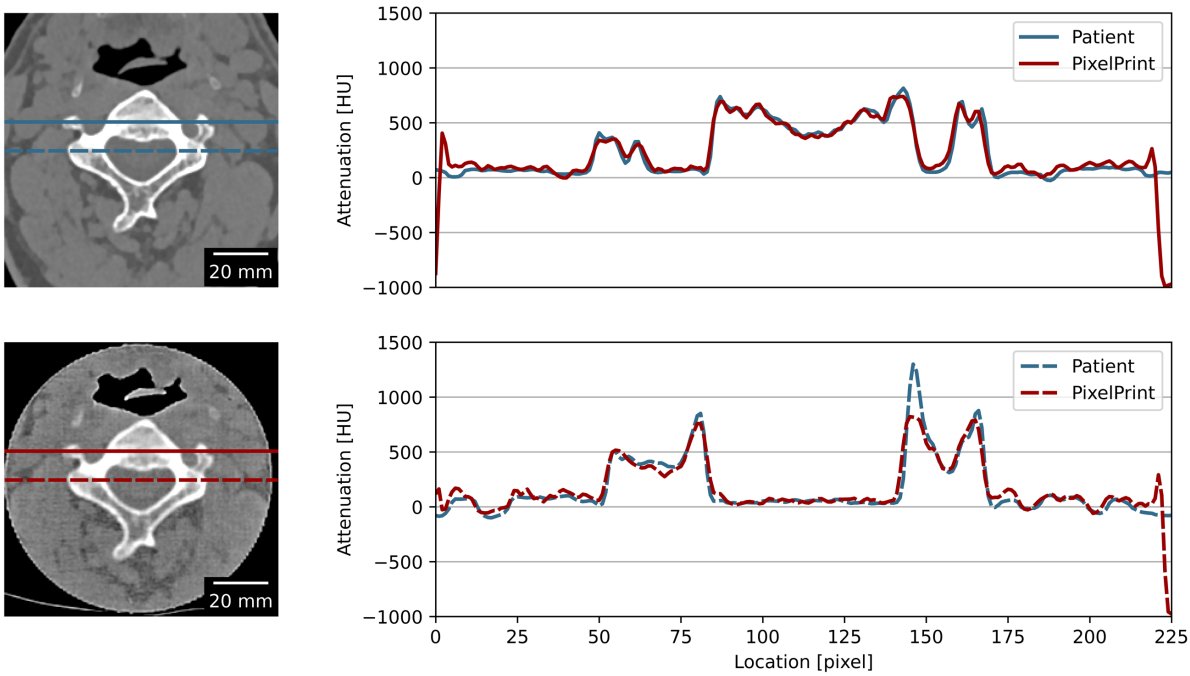

Figure 5. Line profiles of the PixelPrint phantom and the patient CT images. Images on the left show the CT images of the phantom (upper) and the patient images (lower). Red and blue lines indicate the location used to measure the line profile plot on the right. Window level and width are 0 HU and 2000 HU. Images were assumed to be at the same location and registered 2D-wise.

Table 3. Measured Hounsfield units for different tissue types in patient and phantom.

	Area	Patient			PixelPrint Phantom			difference
		mean ± stdev	min	max	mean ± stdev	min	max	
1	Bone I	49.3 ± 31.2	3.4	175.8	57.1 ± 45.5	-45.0	185.3	+7.8
2	Bone II	363.9 ± 50.9	242.2	452.1	349.2 ± 47.0	232.8	504.6	-14.7
3	Cortical Bone	1319.7 ± 87.4	1008.9	1406.8	800.6 ± 14.5	760.6	837.9	-519.0
4	Soft tissue I	55.6 ± 8.5	36.5	76.3	53.1 ± 24.1	5.4	107.3	-2.5
5	Soft tissue II	-78.1 ± 13.5	-105.9	-55.8	-66.2 ± 44.7	-174.9	9.6	+11.9

All measurements are in HUs. Stdev stands for standard deviation. Patient and phantom images were assumed to be the same z location and registered 2D-wise.

Comparable spectral characteristics of the phantom to those of human bone were observed. Figure 6 depicts the spectral attenuation profile of various regions of interest (marked in the left panel) and a 400 mg/ml hydroxyapatite insert (displayed in dark blue in right panel). It is noteworthy that the phantom was fabricated using only one type of filament, and thus, the background, which represents soft tissue, has artificial amounts of calcium.

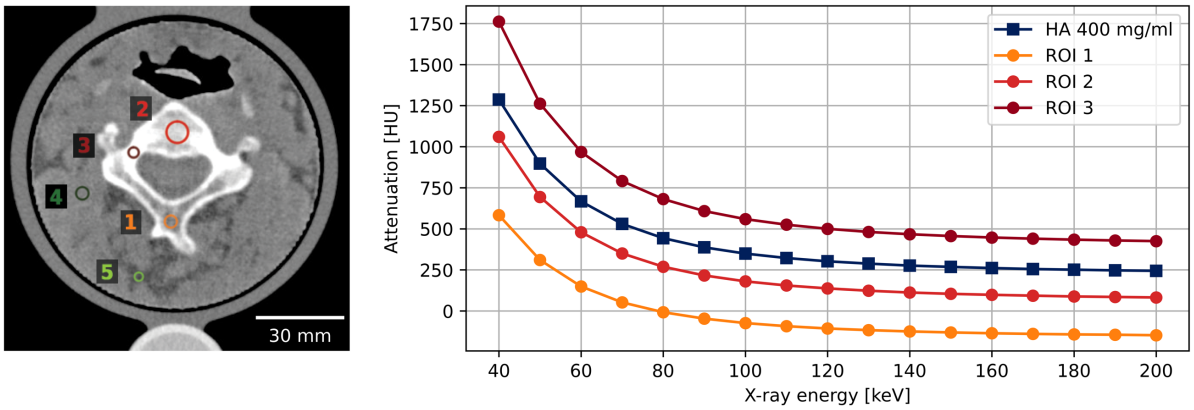

Figure 6. Virtual monoenergetic HU measured with spectral CT. Regions of interest (ROI) are marked in left. Window level and width are 100 and 800 HU. Reference values from a 400 mg/ml hydroxyapatite (HA) insert are marked by dark blue squares.

Discussion

This paper demonstrated how PixelPrint can be utilized to create patient-specific 3D printed bone and soft tissue CT phantoms using one filament. Our approach provides economical and efficient means of producing high resolution CT phantoms, exhibiting excellent accuracy in HU and image texture characteristics in CT scans. These phantoms are useful for a wide range of academic research and clinical evaluation of CT performance.

In contrast to prior studies of image-based 3D printed bone phantoms using slices of the human head/skull [13], chest/thoracic cage [15], pelvis [14] and femoral shaft [6], this study printed the human cervical vertebrae with surrounding soft tissue. Human vertebrae particularly present a

challenging task for 3D printing, as they contain intricate details and are comparatively smaller in size. Nevertheless, these areas, especially in combination with the adjacent tissues, are not only fundamental in clinical diagnostic applications, such as the assessment of severe fractures or degenerative diseases, but also crucial in surgical interventional planning. Our phantoms possess the potential to be utilized for those applications, such as optimizing CT protocols for the assessment of bone mineral density [37] among others. Here, only human cervical vertebrae and knee joint phantoms were printed, but the approach can be extended to any bone structure. With StoneFil filament, a range of approximately -227 HU to 851 HU for a CT scans with a tube voltage of 120 kVp can be reliably printed using PixelPrint, with a deviation of less than 15 HU compared to patient data. This range covers most tissue types in the human body and is applicable to various research applications.

Continuing our previously published research on the PixelPrint lung phantom [18], [19], this study not only extended the types of human tissue printed, but also enhanced the resolution and stability of PixelPrint. Filament line spacing was reduced from 1.0 to 0.5 mm, potentially doubling the resolution capabilities of the printed phantoms. Phantoms produced using this approach can have greater filament coverage and finer details in a given area, serving as valuable tools to evaluate the efficacy of novel higher resolution CT systems such as photon-counting CT [38]–[40]. Printing finer lines with PLA/Stone filament poses more challenges to printer stability control and requires finer system tuning. By optimizing extrusion rate, printing speed, nozzle temperature, and acceleration speed, PixelPrint can still produce highly accurate patient phantoms in reliable stability as demonstrated by qualitative and quantitative evaluation. Additionally, micro-CT acquisitions revealed that filament lines and underlying structure can be generated with high degree of consistency.

With the growing popularity and accessibility of 3D printing technology, a variety of printing filaments are now available for printing human bone and soft tissue. Several studies have

discussed materials for 3D-printed phantoms in CT [24]–[26]. Novel filament materials composed of hydroxyapatite and biocompatible, biodegradable polymers, such as CT-Bone (Xilloc Medical Int., Sittard-Geleen, the Netherlands), can be utilized for printing synthetic bone implants that rapidly induce bone regeneration and growth [41], [42]. Filaments made from composites of fatty acids and ceramic powders have also been explored [28]. However, bone-like filaments available in the general market (FibreTuff, Toledo, OH, USA), suitable for medical surgery purposes [29], [30], do not necessarily have high radiometric densities and are not capable to reach much higher than 400 HU in CT scans. While cancellous bone is only about 300 to 400 HU in CT images, cortical bone can range from 500 HU and up to over 1900 HU [43]. By contrast, materials such as vinyl and PLA with stone (PLA/stone) can offer up to nearly 1000 HU at 96.9% infill ratio at tube voltage of 120 kVp, as they exhibit relatively higher X-ray absorption. Additionally, considering materials for spectral CT phantoms, high impact polystyrene (HIPS) based filaments may be suitable for mimicking CT numbers in applications where energy dependence is important [26], because they show similar spectral profiles as the human body. In this study, we employed StoneFil filament, one type of PLA/stone filament. Unlike normal PLA, StoneFil filament is gravimetrically filled with 50% powdered stones, resulting in significantly higher material density and enabling denser printed objects. Carbonate calcium-containing limestones exhibit a similar X-ray response in CT to that of human bone, whose density can be attributed to hydroxyapatite. This property was reflected in the the spectral response of the printed vertebrae with its similarity to that of hydroxyapatite.

This study has a few limitations: (i) The filament used in our study did not encompass the entire range of Hounsfield Units (HU) required for bone structures. Future research should focus on the development of next-generation filaments that cover the full HU range while preserving spectral capabilities. (ii) The calcium-based material used in the printing process was applied to the entire print, including soft tissue regions. While this approach does not severely impact performance in conventional CT applications, it may have an influence on the evaluation with spectral CT. To

achieve the full dynamic range with spectral characterization for both soft tissue and bone, further development of multiple print head systems will be required. (iii) The printed phantoms were limited to a specific field of view. Future studies should explore the potential to print larger anatomical regions, such as the entire chest or abdomen.

Conclusion

Our study successfully showed the feasibility of using PixelPrint and stone-based filament to 3D-print patient-based bone phantoms with surrounding soft tissue for use in clinical CT applications. The resulting phantoms accurately replicated patient's CT imaging, including precise organ geometry, image texture, and attenuation profiles for spectral CT, which can greatly benefit both academic research and clinical applications.

Acknowledgements

We acknowledge support through the National Institutes of Health (R01CA249538, R01EB030494, and R01EB031592).

References

[1] R. Tino, A. Yeo, M. Leary, M. Brandt, and T. Kron, "A systematic review on 3D-Printed imaging and dosimetry phantoms in radiation therapy," *Technol Cancer Res Treat*, vol. 18, pp. 1–14, 2019, doi: 10.1177/1533033819870208.

[2] V. Filippou and C. Tsoumpas, "Recent advances on the development of phantoms using 3D printing for imaging with CT, MRI, PET, SPECT, and ultrasound," *Med Phys*, vol. 45, no. 9, pp. e740–e760, 2018, doi: 10.1002/mp.13058.

[3] F. Rengier *et al.*, "3D printing based on imaging data: Review of medical applications," *Int J Comput Assist Radiol Surg*, vol. 5, no. 4, pp. 335–341, 2010, doi: 10.1007/s11548-010-0476-x.

[4] M. Leary *et al.*, "Additive Manufacture of Lung Equivalent Anthropomorphic Phantoms: A Method to Control Hounsfield Number Utilizing Partial Volume Effect," *J Eng Sci Med Diagn Ther*, vol. 3, no. 1, 2020, doi: 10.1115/1.4044460.

[5] N. Okkalidis, "3D printing methods for radiological anthropomorphic phantoms," *Physics in Medicine and Biology*, vol. 67, no. 15. Institute of Physics, Aug. 07, 2022. doi: 10.1088/1361-6560/ac80e7.

[6] R. Tino, A. Yeo, M. Brandt, M. Leary, and T. Kron, "The interlace deposition method of bone equivalent material extrusion 3D printing for imaging in radiotherapy," *Mater Des*, vol. 199, p. 109439, 2021, doi: 10.1016/j.matdes.2020.109439.

[7] J. Illi *et al.*, "Translating Imaging Into 3D Printed Cardiovascular Phantoms: A Systematic Review of Applications, Technologies, and Validation," *JACC: Basic to Translational Science*, vol. 7, no. 10. Elsevier Inc., pp. 1050–1062, Oct. 01, 2022. doi: 10.1016/j.jacbts.2022.01.002.

[8] B. A. Hamedani, A. Melvin, K. Vaheesan, S. Gadani, K. Pereira, and A. F. Hall, "Three-dimensional printing CT-derived objects with controllable radiopacity," *J Appl Clin Med Phys*, vol. 19, no. 2, pp. 317–328, 2018, doi: 10.1002/acm2.12278.

[9] C. Hazelaar *et al.*, "Using 3D printing techniques to create an anthropomorphic thorax phantom for medical imaging purposes," *Med Phys*, vol. 45, no. 1, pp. 92–100, 2018, doi: 10.1002/mp.12644.

[10] T. Kairn, S. B. Crowe, and T. Markwell, "Use of 3D Printed Materials as Tissue-Equivalent Phantoms," *IFMBE Proc*, vol. 51, pp. 728–731, 2015, doi: 10.1007/978-3-319-19387-8.

[11] M. Leary *et al.*, "Additive manufacture of custom radiation dosimetry phantoms: An automated method compatible with commercial polymer 3D printers," *Mater Des*, vol. 86, pp. 487–499, 2015, doi: 10.1016/j.matdes.2015.07.052.

[12] N. Okkalidis, "A novel 3D printing method for accurate anatomy replication in patient-specific phantoms," *Med Phys*, vol. 45, no. 10, pp. 4600–4606, 2018, doi: 10.1002/mp.13154.

[13] N. Okkalidis and G. Marinakis, "Technical Note: Accurate replication of soft and bone tissues with 3D printing," *Med Phys*, vol. 47, no. 5, pp. 2206–2211, 2020, doi: 10.1002/mp.14100.

[14] N. Okkalidis, K. Bliznakova, and N. Kolev, "A filament 3D printing approach for CT-compatible bone tissues replication," *Physica Medica*, vol. 102, pp. 96–102, Oct. 2022, doi: 10.1016/j.ejmp.2022.09.009.

[15] K. Bliznakova, N. Okkalidis, N. Dukov, S. Zikopoulos, and Z. Bliznakov, "Application of 3D printed anthropomorphic phantoms for research and educational purposes in digital radiology," *2020 8th E-Health and Bioengineering Conference, EHB 2020*, pp. 30–33, 2020, doi: 10.1109/EHB50910.2020.9280163.

[16] K. Bliznakova *et al.*, "Physical anthropomorphic breast phantoms for X-ray imaging techniques: Manufacturing approach," *2020 8th E-Health and Bioengineering Conference, EHB 2020*, pp. 24–27, 2020, doi: 10.1109/EHB50910.2020.9280109.

[17] N. Dukov *et al.*, "Experimental evaluation of physical breast phantoms for 2D and 3D breast x-ray imaging techniques," in *8th European Medical and Biological Engineering Conference: Proceedings of the EMBEC 2020, November 29–December 3, 2020 Portorož, Slovenia*, 2021, pp. 544–552.

[18] K. Mei *et al.*, "Three-dimensional printing of patient-specific lung phantoms for CT imaging: Emulating lung tissue with accurate attenuation profiles and textures," *Medical Physics*, vol. 49, no. 2. John Wiley and Sons Ltd, pp. 825–835, Feb. 01, 2022. doi: 10.1002/mp.15407.

[19] K. Mei *et al.*, "PixelPrint: a collection of three-dimensional CT phantoms of different respiratory diseases. ," in *SPIE Medical Imaging*, 2023.

[20] K. Mei *et al.*, "PixelPrint: three-dimensional printing of patient-specific soft tissue and bone phantoms for CT," in *7th International Conference on Image Formation in X-Ray Computed Tomography*, 2022, vol. 12304, pp. 545–550.

[21] N. Shapira *et al.*, "PixelPrint: three-dimensional printing of realistic patient-specific lung phantoms for CT imaging," Mar. 2022, p. 31. doi: 10.1117/12.2611805.

[22] N. Shapira *et al.*, "PixelPrint: Three-dimensional printing of realistic patient-specific lung phantoms for validation of computed tomography post-processing and inference algorithms," *medRxiv*, pp. 2022–2025, 2022.

[23] S. G. M. , Y. L. & N. P. B. Hsieh *et al.*, "A dense search challenge phantom fabricated with pixel-based 3D printing for precise detectability assessment ," in *SPIE Medical Imaging*, 2023.

[24] R. Bibb, D. Thompson, and J. Winder, "Computed tomography characterisation of additive manufacturing materials," *Med Eng Phys*, vol. 33, no. 5, pp. 590–596, 2011.

[25] O. L. Dancewicz, S. R. Sylvander, T. S. Markwell, S. B. Crowe, and J. V. Trapp, "Radiological properties of 3D printed materials in kilovoltage and megavoltage photon beams," *Physica Medica*, vol. 38, pp. 111–118, 2017, doi: 10.1016/j.ejmp.2017.05.051.

[26] X. Ma, M. Figl, E. Unger, M. Buschmann, and P. Homolka, "X-ray attenuation of bone, soft and adipose tissue in CT from 70 to 140 kV and comparison with 3D printable additive manufacturing materials," *Sci Rep*, vol. 12, no. 1, p. 14580, Aug. 2022, doi: 10.1038/s41598-022-18741-4.

[27] J. Solc, T. Vrba, and L. Burianova, "Tissue-equivalence of 3D-printed plastics for medical phantoms in radiology," *Journal of Instrumentation*, vol. 13, no. 9, 2018, doi: 10.1088/1748-0221/13/09/P09018.

[28] M. B. Jensen *et al.*, "Composites of fatty acids and ceramic powders are versatile biomaterials for personalized implants and controlled release of pharmaceuticals," *Bioprinting*, vol. 10, Jun. 2018, doi: 10.1016/j.bprint.2018.e00027.

[29] R. (Ross) Salary, "Perspective Chapter: Advanced Manufacturing for Bone Tissue Engineering and Regenerative Medicine," in *Advanced Additive Manufacturing*, I. V Shishkovsky, Ed. Rijeka: IntechOpen, 2022. doi: 10.5772/intechopen.102563.

[30] M. Yu, Y. J. Yeow, L. Lawrence, P. P. Claudio, J. B. Day, and R. Salary, "Characterization of the Functional Properties of Polycaprolactone Bone Scaffolds Fabricated Using Pneumatic Micro-Extrusion," *J Micro Nanomanuf*, vol. 9, no. 3, Sep. 2021, doi: 10.1115/1.4051631.

[31] S. Hatamikia *et al.*, "3D printed patient-specific thorax phantom with realistic heterogenous bone radiopacity using filament printer technology," *Z Med Phys*, vol. 32, no. 4, pp. 438–452, Nov. 2022, doi: 10.1016/j.zemedi.2022.02.001.

[32] S. Hatamikia *et al.*, "Realistic 3D printed CT imaging tumor phantoms for validation of image processing algorithms," *Physica Medica*, vol. 105, Jan. 2023, doi: 10.1016/j.ejmp.2022.102512.

[33] S. K. Goodall, P. Rampant, W. Smith, D. Waterhouse, P. Rowshanfarzad, and M. A. Ebert, "Investigation of the effects of spinal surgical implants on radiotherapy dosimetry: A study of 3D printed phantoms," *Med Phys*, vol. 48, no. 8, pp. 4586–4597, Aug. 2021, doi: 10.1002/mp.15070.

[34] T. Kairn, M. Zahrani, N. Cassim, A. G. Livingstone, P. H. Charles, and S. B. Crowe, "Quasi-simultaneous 3D printing of muscle-, lung- and bone-equivalent media: a proof-of-concept study," *Phys Eng Sci Med*, vol. 43, no. 2, pp. 701–710, 2020, doi: 10.1007/s13246-020-00864-5.

[35] V. Giacometti *et al.*, "3D-printed patient-specific pelvis phantom for dosimetry measurements for prostate stereotactic radiotherapy with dominant intraprostatic lesion boost," *Physica Medica*, vol. 92, pp. 8–14, Dec. 2021, doi: 10.1016/j.ejmp.2021.10.018.

[36] G. Bradski, "The OpenCV Library," *Dr. Dobb's Journal of Software Tools*, 2000.

[37] K. Mei *et al.*, "Is multidetector CT-based bone mineral density and quantitative bone microstructure assessment at the spine still feasible using ultra-low tube current and sparse sampling?," *Eur Radiol*, pp. 1–11, 2017, doi: 10.1007/s00330-017-4904-y.

[38] M. J. Willemink, M. Persson, A. Pourmorteza, N. J. Pelc, and D. Fleischmann, "Photon-counting CT: technical principles and clinical prospects," *Radiology*, vol. 289, no. 2, pp. 293–312, 2018.

[39] S. Si-Mohamed *et al.*, "Review of an initial experience with an experimental spectral photon-counting computed tomography system," *Nucl Instrum Methods Phys Res A*, vol. 873, pp. 27–35, 2017.

[40] L. P. Liu *et al.*, "First-generation clinical dual-source photon-counting CT: ultra-low-dose quantitative spectral imaging," *Eur Radiol*, pp. 1–9, 2022.

[41] Y. Kanno *et al.*, "Computed tomographic evaluation of novel custom-made artificial bones, 'CT-bone', applied for maxillofacial reconstruction," *Regen Ther*, vol. 5, pp. 1–8, Dec. 2016, doi: 10.1016/j.reth.2016.05.002.

[42] A. Hikita, U. Il Chung, K. Hoshi, and T. Takato, "Bone Regenerative Medicine in Oral and Maxillofacial Region Using a Three-Dimensional Printer," *Tissue Eng Part A*, vol. 23, no. 11–12, pp. 515–521, Jun. 2017, doi: 10.1089/ten.tea.2016.0543.

[43] S. Patrick, N. P. Birur, K. Gurushanth, A. S. Raghavan, S. Gurudath, and others, "Comparison of gray values of cone-beam computed tomography with hounsfield units of multislice computed tomography: an in vitro study," *Indian Journal of Dental Research*, vol. 28, no. 1, p. 66, 2017.

Author Contribution

K.M., M.G. and P.N. devised the project, the main conceptual ideas and proof outline. N.S., G.G and J.W. contributed to the design and the research.

K.M. implemented the idea. K.M. P.P. and L.L. performed the experiments and measurements.

457 K.M. analysed the data and wrote the manuscript with support from L.L. and P.N. N.S., G.G and
458 J.W. helped the revision of the manuscript.

459 Additional Information

460 The authors have no relevant conflicts of interest to disclose.

461 Data Availability

462 Datasets generated during this study are available from the corresponding author upon
463 reasonable request.

464